Optical Antenna Properties of Scanning Probe Tips: Plasmonic Light Scattering, Tip−Sample Coupling, and Near-Field Enhancement

Nicolas Behr[†] **and Markus B. Raschke***

Department of Chemistry, University of Washington, Seattle, Washington 98195

Received: October 7, 2007; In Final Form: December 12, 2007

The optical near-field distribution and enhancement near the apex of model scanning probe tips are calculated within the quasistatic approximation. The optical tip−sample coupling sensitively depends on both the tip and sample material. This, in addition to the tip−sample distance and apex geometry, is found to affect the spatial resolution that can be obtained in scattering near-field microscopy (*s*-SNOM). A pronounced structural plasmon resonant behavior is found for gold tips, which redshifts upon tip−sample approach on the length scale given by the tip radius. This near-field tip−sample coupling also allows for surface plasmon excitation in the sample. With the critical dimensions of the tip apex in the range of 10 to several 10s of nanometers, the results are found to be in good agreement with experiment and more rigorous theoretical treatments.

I. Introduction

A wide variety of near-field optical phenomena rely on the local field enhancement and confinement of metallic nanostructures, ranging from the design of subwavelength-size photonic devices[1] to surface-enhanced spectroscopies for sensing applications.[2,3] Similarly, the near-field properties of scanning probe metal tips became increasingly important for the purpose of tip-enhanced or scattering-type near-field microscopy (*s*-SNOM)[4−7] and light emission in scanning tunneling microscopy (STM).[8,9] Combining optical spectroscopy with scanning probe methods, these techniques uniquely allow for optical spectroscopy with ultrahigh spatial resolution down to ∼10 nm.

The reproducible performance of *s*-SNOM experiments, however, has remained challenging. Spatial resolution and signal intensity that can be obtained were found to sensitively depend not only on apex radius but also on tip material and shape.[10] In addition, and akin to other strongly near-field enhanced processes, the local electromagnetic near-field coupling between the tip apex region and the sample surface is important.[7,11] It is ultimately responsible for the imaging contrast and sensitivity that can be obtained. Also, the tip scattered spectral response can become a complex superposition of the tip and sample optical properties, the understanding of which is important in nanospectroscopy.

The near-field distribution and enhancement have been derived for a variety of tip geometries and tip and sample material combinations using different theoretical methods.[12−22] The accurate theoretical treatment of the problem is possible by solving Maxwell's equation numerically.[17,23,24] Although recent calculations closely reproduce the experimental results, the approach is computationally very demanding. Also, it has remained difficult to extract the underlying relevant microscopic parameters responsible for the optical response observed, given that the effects of tip geometry (in terms of, e.g., apex radius and cone angle), tip material, tip−sample distance, and optical wavelength are coupled.

Here, we represent the tip as a hyperboloid chosen as the model geometry, positioned at variable position with respect to the sample surface. We derive systematically how the different dielectric and structural parameters influence the signal characteristics. Taking advantage that the experimentally relevant dimensions of the tip apex are in the 10 nm range, we can treat the problem in the quasistatic approximation that allows solving the Laplace equation analytically. This provides the electrostatic potential and thus the distribution of the local optical electric field at the apex region. In contrast to purely numerical techniques, this approach provides direct insight into how the solution scales with the different geometric, material, and optical parameters. The results prove to be sufficiently accurate for most practical purposes as we will show from comparison with experimental results.[5,7,10,11,24,25]

By varying the tip material and apex radius, we find that for free-standing tips the local-field enhancement is quite moderate with typical values not exceeding 20−40 even for metal tips excited at their plasmon resonance frequency and with apex radii of 10 nm. In contrast, the enhancement can increase by several orders of magnitude for strong optical coupling for metal tips approaching a metal sample with a near powerlaw distance dependence. The lateral confinement of the field enhancement in the tip−sample gap is notably dependent on the sample material, an effect that influences the spatial resolution in tip-scattering near-field experiments. The spectral response depends on the tip shape and material, with a pronounced plasmon resonant behavior found for gold tips. The tip plasmon resonance shifts to longer wavelengths for the tip approaching the surface on a length scale given by the apex radius. Conversely, the presence of nonplasmonic tips such as tungsten near the surface allows for the excitation of a, albeit weaker, surface plasmon in, for example, a gold sample that is otherwise forbidden by wave-vector conservation.

II. Method

A. Tip−Sample Geometry. The tip−sample geometry consists of the tip positioned above the sample plane as indicated schematically in Figure 1. The illumination with an external

---

* Corresponding author. E-mail: raschke@chem.washington.edu.
† Present address: Max-Planck-Institut for Gravitational Physics, D-14476 Golm, Germany.
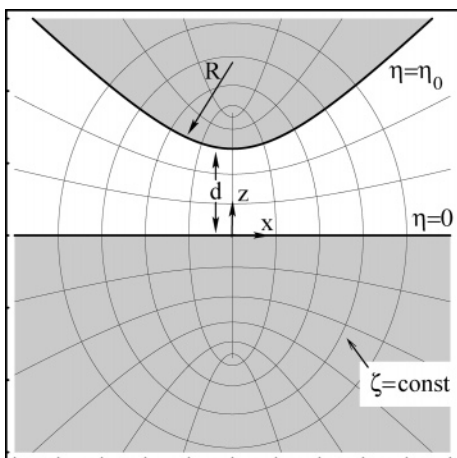
Figure 1. Cross section of tip−sample geometry. The tip with apex radius R is represented by a hyperboloid in prolate spheroidal coordinates ($\eta = \eta_0$) at a distance d above the sample plane ($\eta = 0$). The bold solid lines indicate the tip and sample surface.

light source is modeled by an optical plane wave field polarized parallel with respect to the tip axis.

The parameters for this configuration are the frequency-dependent dielectric functions of the tip material $\tilde{\epsilon}_1$, the medium between tip and surface $\tilde{\epsilon}_2$, and of the planar semiinfinite substrate $\tilde{\epsilon}_3$, as well as the separation distance d between the tip and surface, and the tip apex radius R.

To derive the electrostatic potential, we solve the Laplace equation in the quasistatic approximation. Although the applied optical field of the illuminating light source is in fact a time-varying field, we consider the dimensions of the relevant structural parameters (tip radius, tip−surface distance) to be sufficiently small so that retardation effects can be neglected. This implies that the electric field has the same amplitude and phase across the entire structure at any time; that is, it can be treated as a static field.[1] The optical wavelength dependence is explicitly taken into account considering the frequency depend-ent on the dielectric functions of the different media $\epsilon(\omega) = \epsilon_1 + i\epsilon_2$. $\epsilon(\omega)$ is considered to be homogeneous for the three media, with a discontinuous change at the solid interfaces, and independent of the optical wave-vector (local approxima-tion).

In order to formulate an analytically solvable problem, we approximate the experimental geometry using the prolate ellipsoidal coordinate system. Here, the tip is assumed to have the shape of a rotationally symmetric hyperboloid with apex radius R and semiangle θ. Hence, the 3D problem reduces to one in 2D with the Cartesian coordinates x and z given by

$$x = k \sqrt{(\zeta^2 - 1)(1 - \eta^2)} \tag{1}$$

$$z = k\zeta\eta \tag{2}$$

with the spheroidal coordinates ζ and η, and $1 \leq \zeta \leq \infty$ and $-1 \leq \eta \leq 1$, and the scaling parameter k. The surface plane and tip surface are described by $\eta = 0$ and $\eta = \eta_0$, respectively (see Figure 1). Then, the parameter k and the tip−surface separation d are correlated by $d = k\eta_0$. Similarly, d, η_0, and tip apex radius R are related and cannot be chosen independently[26]

$$R = d\left(\frac{1}{\eta_0{}^2} - 1\right) \tag{3}$$

with $\eta_0 = \cos\theta$. Despite this constraint of the prolate ellipsoidal coordinate system, the model is applicable to a wide range of realistic experimental tip−sample geometries.

B. Solution of the Electrostatic Problem. We search for solutions of the two-dimensional Laplace equation $\Delta\phi = 0$ for the electrostatic potential ϕ. In prolate ellipsoidal coordinates, the Laplace equation is separable and has the general solution[27]

$$\phi = R(\zeta)H(\eta) \tag{4}$$

with

$$R(\zeta) = r_1 P_\nu(\zeta) + r_2 Q_\nu(\zeta) \tag{5}$$

$$H(\eta) = h_1 P_\nu(\eta) + h_2 Q_\nu(\eta) \tag{6}$$

Here, r_i, h_i, $\nu \in \mathcal{C}$, and P_ν, Q_ν denote the Legendre functions of degree ν of first or second kind, respectively.[49] The Legendre functions $P_\nu(x)$ and $Q_\nu(x)$ fulfill the general relations (cf. ref 28)

$$P_\nu(x) = P_{-\nu-1}(x) \tag{7}$$

$$Q_\nu(x) = Q_{-\nu-1}(x) \tag{8}$$

$$P_\nu(x \to 1) \propto 1 + \mathcal{O}(x) \tag{9}$$

$$Q_\nu(x \to 1) \propto \left(\frac{1}{2}(\log(1+x) - \log(1-x)) - \Psi(1+\nu)\right) \times (1 + \mathcal{O}(x)) + ... \tag{10}$$

$$P_\nu(x \to \infty) \propto x^\nu \tag{11}$$

$$Q_\nu(x \to \infty) \propto x^{-\nu-1} \tag{12}$$

where Ψ denotes the polygamma function. The solution of the form of eq 4 has to be analytical over the whole coordinate space. If the argument of a Legendre function of second kind approaches 1, then the function shows a logarithmic divergence as seen from the series expansion in eq 10. Therefore, with $x = \zeta$ and $x = \eta$, neither $R(\zeta)$ nor $H(\eta)$ can contain Legendre functions of the second kind (i.e., $r_2 = h_2 = 0$).

In addition, outside the tip−sample interaction region the optical field E_0 remains constant and polarized in the z direction. This demands solutions for the potential that are at most linear in $z = k\zeta\eta$ far from the tip apex, which implies $\nu \leq 1$. With $P_\nu(x) = P_{-\nu-1}(x)$ (eq 7), this restricts the parameter ν further to $\nu \geq -0.5$. That restriction also insures the uniqueness of the solution for a given geometric configuration.

In summary, one arrives at the following ansatz for the three regions consisting of tip surface (I), space between tip and surface (II) and semiinfinite substrate (III):

$$\phi_\mathrm{I} = P_\nu(\eta)\, P_\nu(\zeta) \tag{13}$$

$$\phi_\mathrm{II} = (aP_\nu(\eta) + bP_\nu(-\eta))P_\nu(\zeta) \tag{14}$$

$$\phi_\mathrm{III} = cP_\nu(\eta)\, P_\nu(\zeta) \tag{15}$$

with a, b, $c \in \mathcal{C}$ and neglecting an overall scaling factor ϕ_0. The free parameters a, b, c, and ν can be derived from the four boundary conditions both at the tip apex ($\eta = \eta_0$)

$$\phi_\mathrm{I}(\eta_0) = \phi_\mathrm{II}(\eta_0) \tag{16}$$

$$\tilde{\epsilon}_1 \partial_\eta \phi_\mathrm{I}|_{\eta=\eta_0} = \tilde{\epsilon}_2 \partial_\eta \phi_\mathrm{II}|_{\eta=\eta_0} \tag{17}$$

and at the surface plane ($\eta = 0$)

$$\phi_{\text{II}}(0) = \phi_{\text{III}}(0) \qquad (18)$$

$$\tilde{\epsilon}_2 \partial_\eta \phi_{\text{II}}|_{\eta=0} = \tilde{\epsilon}_3 \partial_\eta \phi_{\text{III}}|_{\eta=0} \qquad (19)$$

with $\tilde{\epsilon}_i$ denoting the complex dielectric functions of media I, II, and III, respectively. From the first three equations, explicit solutions for parameters a, b, and c (still depending on ν), derive as

$$a = \frac{\tilde{\epsilon}_1 \alpha(\nu_0, \eta_0) + \tilde{\epsilon}_2 \beta(\nu_0, \eta_0)}{\tilde{\epsilon}_2 (\alpha(\nu_0, \eta_0) + \beta(\nu_0, \eta_0))} \qquad (20)$$

$$b = \frac{\tilde{\epsilon}_2 - \tilde{\epsilon}_1}{\tilde{\epsilon}_2 (\alpha(\nu_0, \eta_0) + \beta(\nu_0, \eta_0))} \qquad (21)$$

$$c = \frac{\tilde{\epsilon}_1 (\alpha(\nu_0, \eta_0) - 1) + \tilde{\epsilon}_2 (\beta(\nu_0, \eta_0) + 1)}{\tilde{\epsilon}_2 (\alpha(\nu_0, \eta_0) + \beta(\nu_0, \eta_0))} \qquad (22)$$

Here, ν_0 denotes the ν value solving the fourth boundary condition

$$(\tilde{\epsilon}_2 - \tilde{\epsilon}_1) \frac{\tilde{\epsilon}_2 - \tilde{\epsilon}_3}{\tilde{\epsilon}_2 + \tilde{\epsilon}_3} - \tilde{\epsilon}_1 \alpha(\nu, \eta_0) - \tilde{\epsilon}_2 \beta(\nu, \eta_0) = 0 \qquad (23)$$

and the auxiliary functions α and β are defined as

$$\alpha(\nu, \eta) \equiv P_\nu(-\eta)/P_\nu(\eta) \qquad (24)$$

$$\beta(\nu, \eta) \equiv P'_\nu(-\eta)/P'_\nu(\eta) \qquad (25)$$

with prime denoting the derivative with respect to η.

In order to calculate the resulting electrostatic field from the potential described by eq 4, we transform the solution into Cartesian coordinates[50] and take the spatial derivatives. To add a physical meaning to the so far dimensionless electric field, we have to provide a suitable normalization factor. Throughout this work, we are interested in the relative field strengths near the tip apex with respect to the unperturbed incident field. Therefore, we define the potential difference between two arbitrary points sufficiently far outside the tip−sample interaction region to define the reference electric field strength

$$E_0 = \frac{\phi(x_1, z_1) - \phi(x_2, z_2)}{\sqrt{(x_1 - x_2)^2 + (z_1 - z_2)^2}} \qquad (26)$$

It is convenient to choose the Raleigh length $\lambda/2\pi$ for the reference distance $x_{\text{ref}} = x_1 - x_2 = 100$ nm $\approx \lambda/2\pi$ with λ denoting the wavelength of the illuminating light (here $\lambda = 630$ nm). Similarly $z_{\text{ref}} = z_2 - z_1 \equiv d_{\text{min}}$ with d_{min} denoting the minimal tip−surface separation of the configurations under consideration. Here, $d_{\text{min}} = 2$ nm was chosen to cover typical atomic-force microscopy distances relevant for s-SNOM.

C. Computation. Calculations for different tip shapes, tip−sample distances, and tip and sample materials are performed using Mathematica.[29] No more than a few minutes computation time is required on, for example, a 1 GHz Intel PC CPU, for each geometric configuration. The calculations are performed on a grid with 201×121 points. For the complex dielectric constants of different wavelengths, experimental values are used. For calculations of different materials at fixed wavelengths as well as the spectroscopic response of W, $\tilde{\epsilon}(\omega)$ is taken from ref 30. For the wavelength-dependent calculations of Au, the
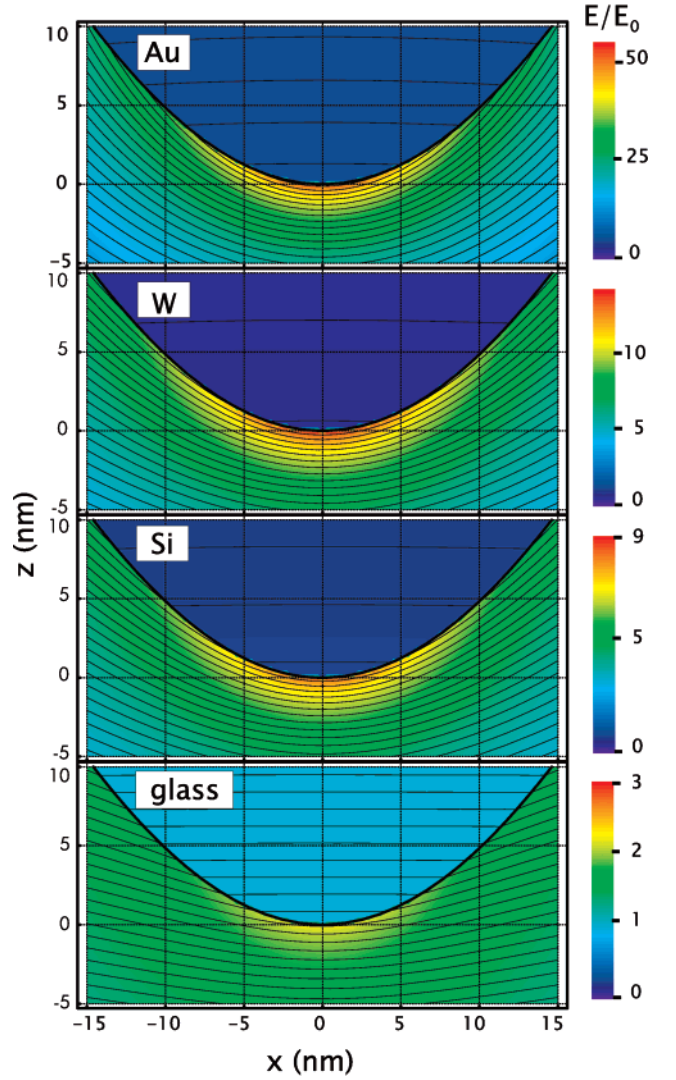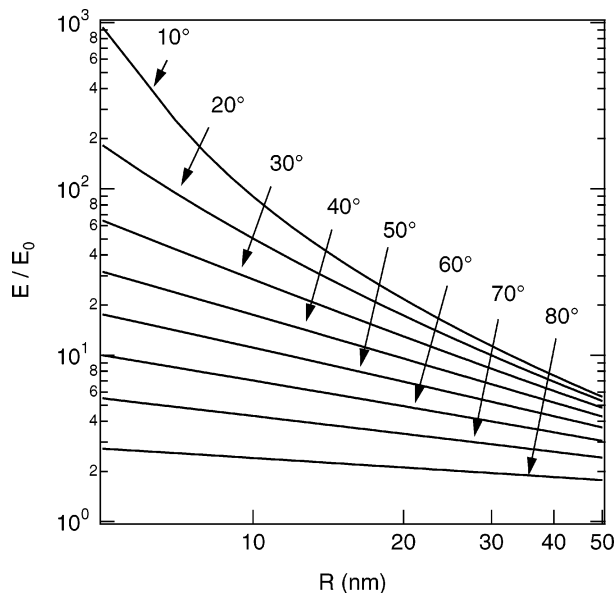

Figure 2. Dependence of field enhancement (E/E_0) on tip material for free-standing tips with apex radius $R = 10$ nm, cone semiangle of $\theta = 20°$, and wavelength $\lambda = 630$ nm. The solid lines represent contours of constant potential.

empirical model function for $\epsilon(\omega)$ from ref 31 is used that is based on the experimental data of ref 32.

III. Results

A. Free-Standing Tips. Figure 2 shows characteristic local field distributions and corresponding enhancement near the apex region for four free-standing tips of different tip materials: gold (a), tungsten (b), silicon (c), and glass (d). A hyperboloid with apex radius $R = 10$ nm and cone semiangle of $\theta = 20°$ was chosen. For the incident field with wavelength $\lambda = 630$ nm, the corresponding dielectric constants used are about $\epsilon_{\text{Au}} = -9.90 + 1.05i$, $\epsilon_{\text{W}} = 5.05 + 21.8i$, $\epsilon_{\text{Si}} = 12.1 + 1.04 \times 10^{-8}i$, and $\epsilon_{\text{glass}} = 2.25$.[30]

The solid lines represent contours of constant potential. At optical frequencies, even for metals the tip surface does not represent an equipotential surface—in contrast to the electrostatic case. The finite response time of the charge carriers with respect to the optical frequency results in the decay of the field inside the tip on the length scale given by the skin depth. For gold as a representative material with high conductivity, this results in the strongest field enhancement of $E/E_0 \approx 50$ at the apex. In contrast, tungsten as a common scanning probe tip material is a poor conductor in the optical frequency range leading to a

Optical Antenna Properties

J. Phys. Chem. C, Vol. 112, No. 10, 2008 **3769**

Figure 3. Dependence of field enhancement (E/E_0) near the apex on tip-radius R and tip-semiangle θ for gold tips at $\lambda = 630$ nm.

comparably moderate enhancement of ~12. Its values are only slightly above what is found for silicon. This behavior for tungsten and silicon is characteristic of materials with strong damping due to absorptive loss. Transparent dielectrics with small indices of refraction have the weakest field enhancement as shown here for the case of glass.

The degree of field enhancement at the tip apex sensitively depends on both apex radius R and semiangle θ of the tip. This correlation is shown in Figure 3 for the case of gold at an excitation wavelength of 630 nm with values for E/E_0 ranging between 10 and 100 for typical tips with 10−20 nm radius and realistic semiangles.

Note that for these and the following calculations that refer to the field at the tip (Figure 3, 8, and 9) the field is evaluated at 0.125 nm below the tip apex. This avoids unwanted numerical artifacts due to the finite grid size.

B. Tip−Sample Coupling. The local field enhancement as well as the lateral confinement can change significantly for the tip in close proximity to a surface plane. This behavior is of crucial importance for the contrast in scattering near-field microscopy. The optical tip−sample coupling is the result of the forcing of the boundary conditions at the surface plane on the field emerging from the apex. This gives rise to a mutual and constructive tip−sample optical polarization for the electric field oriented parallel with respect to the tip axis. The effect is therefore most pronounced for metallic tips and substrates. Figure 4 shows the case for a gold tip ($R = 10$ nm, initial $\theta = 45°$) near a gold surface for two representative distances of 10 and 5 nm. As can be seen, the tip−sample approach is accompanied by a significant increase in field enhancement in the tip−sample gap.

For a tip−sample distance of $d = 5$ nm, Table 1 summarizes the values for the field enhancement determined near the sample surface underneath the tip (i.e., $x = 0$ nm, $z = 0.125$ nm) for different tip and sample material combinations.

Note that, as discussed above, the increase in cone angle with decreasing tip−sample distance for a given tip radius seen in Figure 4 is the result of the correlation between distance d, apex radius R, and semiangle θ as given by eq 3. Although this limits the quantitative analysis, important general qualitative conclusions can be drawn. For that purpose, it is illustrative to discuss
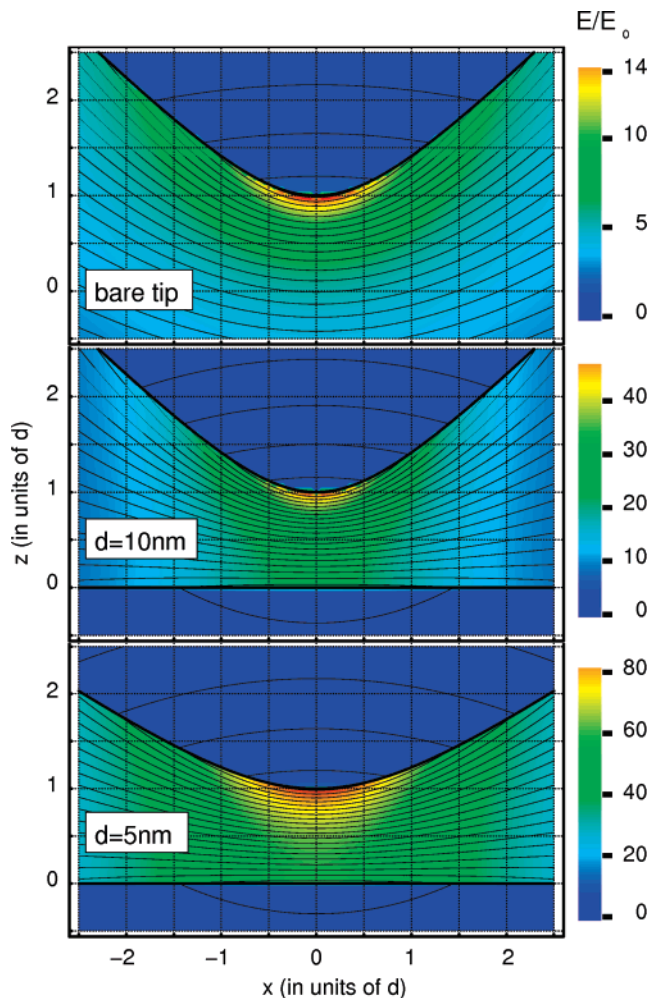

Figure 4. Spatial distribution and variation of field enhancement (E/E_0) with tip−sample separation for Au tip and substrate with apex radius $R = 10$ nm and $\lambda = 630$ nm. Note that the initial cone angle of $\theta = 45°$ increases with decreasing distance according to eq 3.

TABLE 1: Field Enhancement near the Sample Surface Plane at $z = 0.125$ nm and $x = 0$ nm for Different Tip−Substrate Material Combinations for Tips with $R = 10$ nm and $\theta = 45°$ at $d = 5$ nm

surface	Au tip	W tip	Si tip	glass tip
Au	49.8	14.2	9.2	2.5
W	25.4	10.1	7.1	2.3
Si	19.6	8.7	6.2	2.2
glass	8.4	5.0	3.9	1.8

the evolution of the field in the tip−sample gap calculated along the axial direction for different distances (Figure 5). For a tip with $R = 10$ nm and the largest distance of $d = 40$ nm, the variation in field strength with distance from the apex resembles that of a free-standing tip. The tip−sample interaction is correlated with apex radius and only becomes significant at distances below about twice the tip radius (here, $d = 20$ nm) when the near-field interaction becomes effective. The field enhancement then starts to rise superexponentially for distances below the apex radius ($d = 10$ nm) with a particularly fast rise of the field at the sample surface. Considering the corresponding increase in cone angle with decreasing distance, the enhancement E/E_0 of up to several hundred at $d = 2$ nm might underestimate what one would obtain for a fixed cone angle, and should therefore be seen as a lower limit.

In addition, a decreasing tip−sample distance is associated with a strong lateral confinement of the field. The equipotential
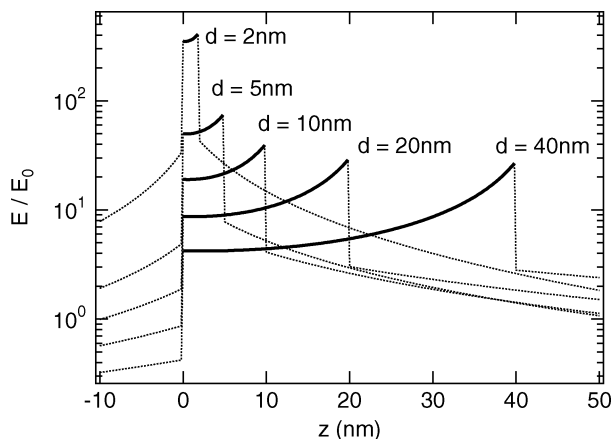
Figure 5. Variation of field enhancement E/E_0 along the axial direction across the Au tip−Au sample gap region ($x = 0$ nm) for different distances d at an excitation wavelength $\lambda = 630$ nm. The tip ($R = 10$ nm) is at variable $z = d$ positions and extends to the right. The sample surface is located at $z = 0$ nm, and its bulk occupies the range of negative z values.
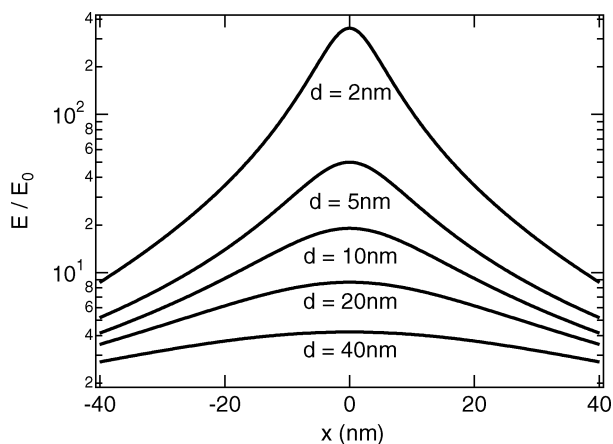

Figure 6. Lateral cross section near the sample surface ($z = 0.125$ nm) for different tip−sample distances for a gold tip ($R = 10$ nm) above a gold surface.

surface is forced to align close to parallel with the substrate plane, which gives rise to an enhanced lateral concentration of the field. Figure 6 shows linear cuts along the x direction near the sample plane ($z = 0.125$ nm) for different tip−sample distances. The half width is not only correlated with apex radius but also strongly depends on tip−sample distance with a fwhm decreasing from 65, to 38, 24, and 12 nm for tip sample distances of $d = 20$, 10, 5 and 2 nm, respectively. This has important consequences such as an expected increase in spatial resolution in scanning probe near-field microscopy for small tip−sample distances as discussed below. In addition, because of the differences in boundary conditions at the sample surface the fwhm varies with sample material, that is, decreases with decreasing optical polarizability of the material.

C. Spectroscopic Properties. One of the virtues of the quasistatic model is the direct access to the spectral variation of the field distribution for different tip−sample geometries. For a Au tip ($R = 10$ nm, initial $\theta = 45°$) approaching a Au surface, Figure 7 shows the calculated spectral dependence of the field enhancement near the surface ($x = 0$ nm, $z = 0.125$ nm). As expected, a structural plasmon resonant behavior is observed. Associated with the increasing enhancement for shorter distances, one observes a shift in the plasmon response to longer wavelengths. This redshift is especially pronounced for distances $d \leq R$, that is, correlated with
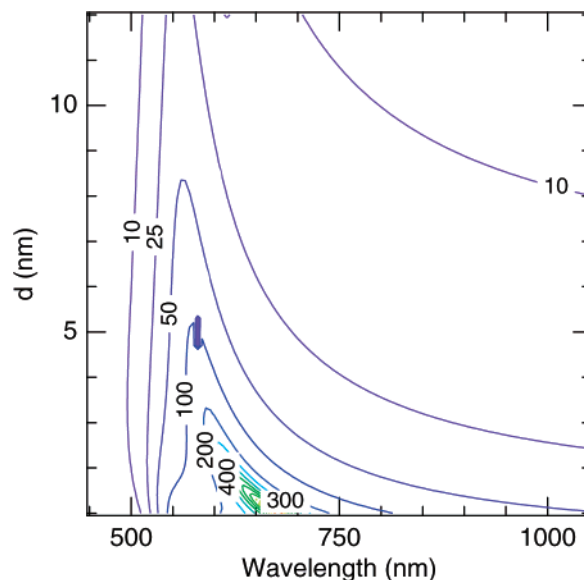
Figure 7. Spectral dependence of field enhancement with tip−sample distance d for a Au tip ($R = 10$ nm) approaching a Au surface. The pronounced redshift of the plasmon response is associated with the strong near-field tip−sample coupling for $d \leq R$. The lines represent contours of equal optical field enhancement.
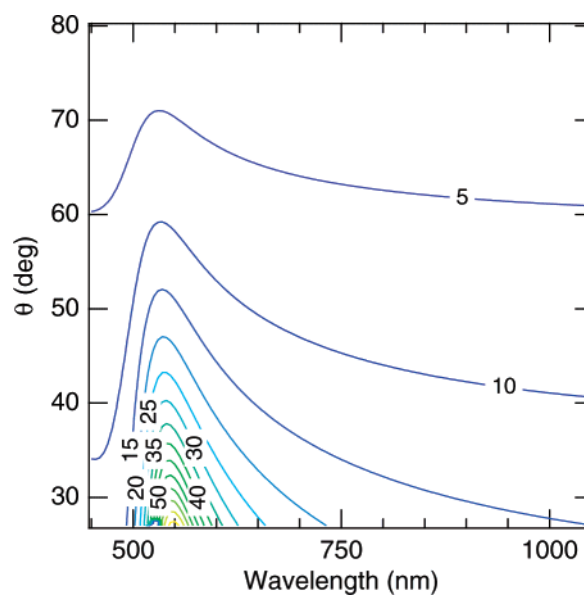

Figure 8. Plasmon response expressed in terms of the field enhancement near the tip apex for a bare Au tip ($R = 10$ nm) with varying semiangle θ.
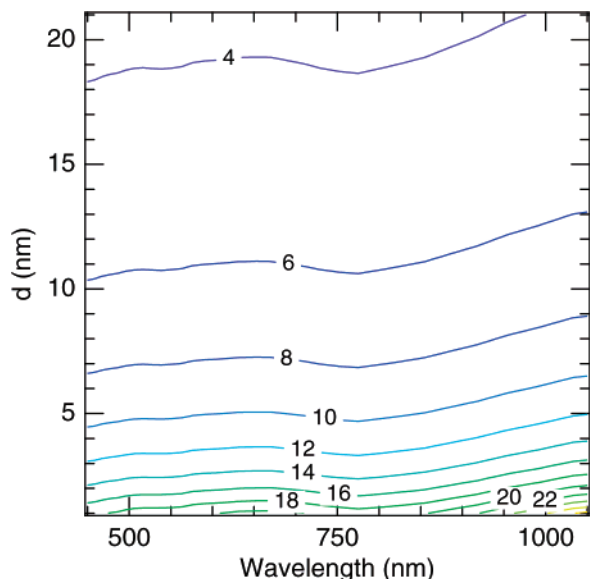
the onset of the sharp rise in field enhancement as discussed above and a manifestation of the regime of strong coupling. (The anomaly in the contour for the field enhancement of ∼100 at $\lambda \sim 580$ nm and $d \sim 5$ nm is a computational artifact.)

Although the decrease in tip−sample distance is necessarily associated with an increase in cone angle as discussed above, the spectral shift observed can nevertheless be attributed to the effect of the increase in tip−sample coupling for shorter distances. This is concluded from studying the effect of the variation of the cone angle itself on the spectral response for a bare tip.

As seen in Figure 8 for a Au tip with fixed apex radius $R = 10$ nm, the increase in cone angle does not affect the spectral position of the plasmon response. It only affects the degree of field enhancement at the apex as expected.
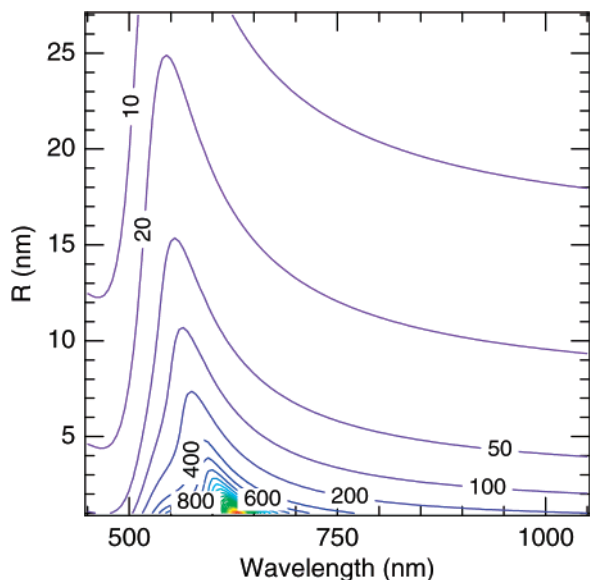
Figure 9. Spectral red shift of the plasmon response for a bare Au tip evaluated near the apex with decreasing radius R for a fixed semiangle of $\theta = 20°$.

Figure 11. Spectral and tip−sample distance dependence of the near-apex field of a W tip approaching a Au surface. The loss in translational invariance due to the presence of the (nonresonant) tip allows for the surface plasmon polariton excitation in the metal film otherwise forbidden by wave-vector conservation.
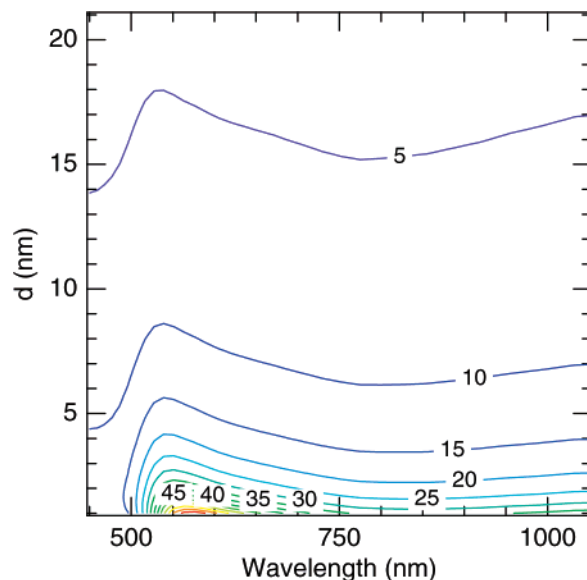

Figure 10. Spectral and distance dependence of the field enhancement for a W tip ($R = 10$ nm) approaching a W surface. The spectrally flat response and the moderate field enhancement even for short distances are characteristic for a nonplasmon resonant behavior.

In contrast, the variation in apex radius for a bare tip at fixed semiangle θ gives rise to a shift in the plasmon response. As seen in Figure 9 for a tip with $\theta = 20°$, a decrease in apex radius is accompanied by a red shift of the tip plasmon.

Using W as the tip material, no plasmon resonant behavior is observed. Figure 10 shows the result for a W tip with apex radius $R = 10$ nm approaching a W surface. The spectrally flat response and moderate field enhancement are expected because W does not support a surface plasmon polariton in the visible spectral range. Similar spectral results, although with lower values of the field enhancement, are obtained for the bare tip by varying the apex radius or semiangle (data not shown).

Notably, a plasmon resonant behavior can be observed by combining a nonresonant tip with a resonant substrate material. The result obtained for a W tip ($R = 10$ nm) approaching a Au surface is shown in Figure 11. Because of the reduced mutual tip−sample polarization, the plasmon response between 550 and

600 nm is much weaker compared to the Au-tip/Au-surface combination and only exhibits a comparably small spectral shift for close distances. The moderate rise in enhancement above 800 nm is due to the spectral behavior of W as can be seen from comparison with the W-tip/W-surface result shown in Figure 10. The details of the excitation mechanism that gives rise to this plasmonic tip-scattering response from a nonplasmonic tip are discussed in detail below.

IV. Discussion

A. Field Enhancement. The results for the field enhancement calculated for the bare tips as well as its variation with tip−sample distance are found to be in good agreement with recent detailed theoretical studies and experimental observations. Using a fully 3D finite-difference time-domain (FDTD) method, the field distribution has been calculated[24] with similar results obtained in refs 19, 20, and 33. For Au tips with apex radii of 10 nm, excitation wavelengths of 633 nm, and the fields parallel to the tip axes, that is, parameters comparable to the ones considered above, field enhancements between 10 and 20 are found for the bare tips.[24] Within the uncertainty given by the numerical accuracy especially at the tip surface boundaries due to the finite 3D grid used, this is in full agreeement with the quasistatic calculation shown in Figure 4. In the presence of a Au surface at a distance of $d = 8$ nm, the FDTD calculation provides an enhancement factor of ~60 for the field near the tip apex and ~40 near the surface. These results are in accordance with the range of values given by the geometries with $d = 5$ and $d = 10$ nm considered here. In addition, the FDTD calculations for the tip−sample distance dependence and the field variation inside the tip−sample gap result in field strengths and distributions of values comparable to the ones derived using the quasistatic model.

These results support the validity of the quasistatic approach for the limiting case of small apex dimensions as discussed in the introduction. Both in the FDTD calculations and in the experiments, the tips are in general more slender than a hyperboloid. However, as this work suggests from the good agreement between the quasistatic hyperboloidal model, the

FDTD calculations with a more narrow cone, and the experimental results, the response is more sensitive with respect to apex radius rather than the cone angle. This is also in accordance with the comparison of the data shown in Figures 8 and 9, which indicates that a change in semiangle leads to a weaker variation in enhancement when compared to the effect of apex radius within the experimentally relevant ranges.

The theoretical results presented here agree with experiments. For bare Au and W tips the local field enhancement could be derived by tip-scattering second-harmonic generation (SHG). For a pump and SHG radiation of 800 and 400 nm, respectively, and tip radii of $r \sim 20$ nm, values of 8−14 for Au and 3−6 for W could be estimated.[25] Considering that these values correspond to a spatial average over the apex region, this result falls well within the range of predicted values given in Figure 2 for both Au and W. It should be noted that the relative contributions to the total enhancement by the pump and second-harmonic output wavelength could not be distinguished.

The determination of the field enhancement for a tip−sample coupled system has been achieved by tip-enhanced Raman scattering from the surface monolayers of molecular adsorbates.[5,7,24,34,35] From tip−sample distance-dependent Raman measurements in comparison with corresponding far-field experiments, using malachite green dye molecules or single-walled carbon nanotubes (SWNT) local field enhancements of 60−150 at the sample surface and a pump wavelength of 633 nm were measured.[7,24] With the tip−sample distance in the range of just several nanometers, these experimental values are in good agreement with the theoretical values ranging from ∼50 to ∼300 calculated here for distances of 5 to 2 nm. Furthermore, the experimental distance dependences found for the enhancement are in accordance with the theoretical expectations based on Figure 5 and they confirm the correlation of the distance dependence with apex radius as the characteristic length scale.

B. Spectral Response. The excitation of the localized surface plasmon polariton (SPP) in the tip axial direction is responsible for the large field enhancement observed experimentally for Au tips.[5,7,34] In addition, the SPP manifests itself directly in linear Rayleigh scattering spectra from the apex of free-standing Au tips.[10] Depending on the details of the tip geometry, a strongly plasmon resonant emission is observed with peak positions ranging between 550 and 750 nm. Spectral peak widths on the order of 0.2 to 0.3 eV correspond to what is expected from the electronic dephasing times for SPP in Au of $\tau \sim 10-20$ fs.[36]

Although peak positions for bare tips between 550 and 650 nm would be consistent with the hyperboloid tip model described here, the experimentally observed peaks at longer wavelengths are at variance with the range of possible values within the quasistatic theoretical framework, irrespective of apex radius and semiangle (see Figures 7 and 9). One possible interpretation is that the quasistatic model neglects phase retardation, which can give rise to a more complex spectral response.[37] Here, multipole excitation can lead to spectral broadening and/or additional spectral peaks.

Modeling the tip as a hemispheroid,[10,38,39] a continuous shift of the resonance to longer wavelengths is found with increasing aspect ratio. Likewise, using truncated conical structures[21,24] the resonance red shifts with decreasing cone angle. It remains to be shown to which extent this more pronounced sensitivity of the redshift of the structural resonance in these cases is due to the three-dimensionally confined nature of the model tip geometry.

For W, a weak scattering response in the visible spectral region with only a small wavelength dependence was observed experimentally,[25] together with the weak field enhancement discussed above.[10] These results are consistent with the calculated response for W shown in Figure 10, which is characterized by a largely spectrally flat response.

With regard to the near-field coupled tip−sample system, the associated redshift of the plasmon response found in our calculations and shown in Figure 7 for the case of a Au tip approaching a Au surface is a general phenomenon. It is found in calculations of spheres and other plasmonic nanostructures in close proximity to a metal surface.[17,18,39,40] To the best of our knowledge, no corresponding spectrally resolved optical tip-scattering experiments have yet been performed for the near-field coupled tip−sample system. However, light emission in inelastic scanning tunneling microscopy (STM) can provide complementary insight. In that case, rather than by optical excitation, the radiating optical dipole is induced by the inelastic tunneling process. Its radiative spectral characteristic is an equivalent measure for the optical response of the tip−sample coupling. Already in early experiments using W tips and a Au surface, a peak shift from ∼500 to ∼600 nm under tunneling conditions with a tip−sample distance of ∼0.5 nm was observed.[41,42] This experimental finding would be in very good agreement with our theoretical model and corresponds to the results shown in Figure 11.

This observed plasmonic behavior for a tip−sample combination where the tip itself does not support a plasmon response is particularly interesting. Given the SPP dispersion relation for the planar Au surface, for light incident onto the air/Au interface the surface plasmon cannot be excited due to the wavevector mismatch. The tip as a spatially confined oscillating dipole when optically coupled to the interface gives rise to the formation of a localized hybrid plasmon mode between the flat surface and the subwavelength size tip scatterer, that is, between the propagating SPP surface mode and the dispersion-free localized mode of the tip.[18,43−45] Model calculations show that the tip plasmon is spatially confined on a length scale of $l \propto \sqrt{Rd}$.[43] With the wavevector $k \sim l^{-1}$, the frequency of the coupled resonance then scales as $\omega \propto \omega_0(d/2R)^{1/4}$ as predicted in ref 46; that is, the frequency shifts to longer wavelength with decreasing distance, which is in qualitative agreement with our findings.

The underlying optical tip−sample coupling is due to the mutual tip−sample polarization. The initially driven optical polarization in the tip gives rise to a polarization in the surface plane matching the boundary conditions. This surface field in turn affects the field at the metal tip. Therefore, the spectral characteristics of the radiative tip dipole is the result of a superposition of the dielectric functions of the tip and the sample material and is a manifestation of the optical tip sample coupling.

C. Spatial Resolution. The fwhm in the lateral field enhancement distribution calculated in Figure 6 is found to depend on tip−sample distance as well as sample material. For the tip in very close proximity to the sample ($d \leq R$), a resolution better than the apex diameter can be expected as evident from, for example, a fwhm of 12 nm for $d = 2$ nm. Considering that the light intensity in a linear tip-scattering experiment scales as $(E/E_0)^4$[37] a resolution of just several nanometers can be expected for a tip with just $R = 10$ nm if scanned within a few nanometers from the surface. As a consequence of a stronger lateral field confinement for a metallic versus a dielectric sample material, a higher spatial resolution can be obtained imaging metallic as compared to dielectric surface structural features under otherwise identical experimental conditions.

Optical Antenna Properties

J. Phys. Chem. C, Vol. 112, No. 10, 2008 **3773**

V. Summary

In summary, the comparison with exact theoretical treatments of experimental tip geometries and with experimental results on field enhancement and spectral response validates the approach of treating the scanning tip as a hyperboloid in the quasistatic approximation. Despite the simplicity of the model, the essential optical properties of the tip−sample system are predicted accurately including the spatial variation of the field enhancement, the tip−sample distance dependence of the scattering response, the plasmonic behavior for certain tip and sample materials, as well as the spectral shifts with varying distance. The model is valid as long as retardation and higher order multipole contributions can be neglected. This typically corresponds to the condition of $kR \ll 1$ for wave vector and apex radius.[12,37] The increase in spatial resolution with decreasing tip−sample distance for a given tip radius, as well as the dependence of the spatial resolution on sample material for a given tip, is of high practical relevance for tip-scattering near-field microscopy (*s*-SNOM) and spectroscopy.

References and Notes

(1) Maier, S. A.; Brongersma, M. L.; Kik, P. G.; Meltzer, S.; Requicha, A. A. G.; Atwater, H. A. *Adv. Mater.* **2001**, *13*, 1501.

(2) Schatz, G. C.; Young, M. A.; Duyne, R. P. V. In *Topics in Applied Physics. Surface-Enhanced Raman Scattering: Physics and Applications*; Kneipp, K., Moskovits, M., Kneipp, H.; Springer: New York, 2006; Vol. 103, pp 367−379.

(3) Willets, K. A.; Van Duyne, R. P. *Annu. Rev. Phys. Chem.* **2007**, *58*, 267.

(4) Hillenbrand, R.; Taubner, T.; Keilmann, F. *Nature* **2002**, *418*, 159.

(5) Hartschuh, A.; Sanchez, E. J.; Xie, X. S.; Novotny, L. *Phys. Rev. Lett.* **2003**, *90*, 095503.

(6) Ichimura, T.; Hayazawa, N.; Hashimoto, M.; Inouye, Y.; Kawata, S. *Phys. Rev. Lett.* **2004**, *92*, 220801.

(7) Neacsu, C. C.; Dreyer, J.; Behr, N.; Raschke, M. B. *Phys. Rev. B* **2006**, *73*, 193406.

(8) Nilius, N.; Ernst, N.; Freund, H.-J. *Phys. Rev. B* **2002**, *65*, 115421.

(9) Hoffmann, G.; Maroutian, T.; Berndt, R. *Phys. Rev. Lett.* **2004,** *93*, 076102.

(10) Neacsu, C. C.; Steudle, G. A.; Raschke, M. B. *Appl. Phys. B* **2005**, *80*, 295.

(11) Novotny, L.; Stranick, S. J. *Annu. Rev. Phys. Chem.* **2006**, *57*, 303.

(12) Denk, W.; Pohl, D. W. *J. Vac. Sci. Technol., B* **1991**, *9*, 510.

(13) Martin, O. J. F.; Girard, C. *Appl. Phys. Lett.* **1997**, *70*, 705.

(14) Martin, Y. C.; Hamann, H. F.; Wickramasinghe, H. K. *J. Appl. Phys.* **2001**, *89*, 5774.

(15) Martin, O. J. F.; Paulus, M. J. *Microscopy* **2002**, *205*, 147.

(16) Bouhelier, A.; Renger, J.; Beversluis, M. R.; Novotny, L. *J. Microscopy* **2003**, *210*, 220.

(17) Downes, A.; Salter, D.; Elfick, A. *J. Phys. Chem. B* **2006**, *110*, 6692.

(18) Porto, J. A.; Johansson, P.; Apell, S. P.; Lopez-Rios, T. *Phys. Rev. B* **2003**, *67*, 085409.

(19) Festy, F.; Demming, A.; Richards, D. *Ultramicroscopy* **2004**, *100*, 437.

(20) Downes, A.; Salter, D.; Elfick, A. *Opt. Express* **2006**, *14*, 5216.

(21) Goncharenko, A. V.; Dvoynenko, M. M.; Chang, H.-C.; Wang, J.-K. *Appl. Phys. Lett.* **2006**, *88*, 104101.

(22) Schneider, S. C.; Grafström, S.; Eng, L. M. *Phys. Rev. B* **2005**, *71*, 115418.

(23) Novotny, L.; Bian, R. X.; Xie, X. S. *Phys. Rev. Lett.* **1997**, *79*, 645.

(24) Roth, R. M.; Panoiu, N. C.; Adams, M. M.; Osgood, R. M.; Neacsu, C. C.; Raschke, M. B. *Opt. Express* **2006**, *14*, 2921.

(25) Neacsu, C. C.; Reider, G. A.; Raschke, M. B. *Phys. Rev. B* **2005**, *71*, 201402.

(26) Bronshtein, I. N.; Semendyayev, K. A. *Handbook of Mathematics*; Springer: Berlin, 1985.

(27) Moon, P.; Spencer, D. E. *Field Theory Handbook*; Springer: Berlin, 1971.

(28) http://functions.wolfram.com/HypergeometricFunctions/.

(29) *Mathematica*, version 5.2; Wolfram Research, Inc.: Champaign, IL, 2005.

(30) Palik, E. D., Ed. *Handbook of Optical Constants of Solids*; Academic Press: San Diego, CA, 1985.

(31) Etchegoin, P. G.; Le Ru, E. C.; Meyer, M. *J. Chem. Phys.* **2006**, *125*, 164705.

(32) Johnson, P. B.; Christy, R. W. *Phys. Rev. B* **1972**, *6*, 4370.

(33) Demming, A. L.; Festy, F.; Richards, D. *J. Chem. Phys.* **2005**, *122*, 184716.

(34) Pettinger, B.; Ren, B.; Picardi, G.; Schuster, R.; Ertl, G. *J. Raman Spectrosc.* **2005**, *36*, 541.

(35) Zhang, W.; Yeo, B.; Schmid, T.; Zenobi, R. *J. Phys. Chem. C* **2007**, *111*, 1733, ISSN 1932−7447.

(36) Raether, H. *Surface Plasmons on Smooth and Rough Surfaces and on Gratings*; Springer: Berlin, 1988.

(37) Bohren, C. F.; Huffman, D. R. *Absorption and Scattering of Light by Small Particles*; John Wiley: New York, 1998.

(38) Calander, N.; Willander, M. *J. Appl. Phys.* **2002**, *92*, 4878.

(39) Geshev, P. I.; Klein, S.; Witting, T.; Dickmann, K.; Hietschold, M. *Phys. Rev. B* **2004**, *70*, 075402.

(40) Aravind, P. K.; Nitzan, A.; Metiu, H. *Surf. Sci.* **1981**, *110*, 189.

(41) Berndt, R.; Gimzewski, J. K.; Johansson, P. *Phys. Rev. Lett.* **1991**, *67*, 3796.

(42) Aizpurua, J.; Apell, S. P.; Berndt, R. *Phys. Rev. B* **2000**, *62*, 2065.

(43) Rendell, R. W.; Scalapino, D. J. *Phys. Rev. B* **1981**, *24*, 3276.

(44) Fischer, U. C.; Pohl, D. W. *Phys. Rev. Lett.* **1989**, *62*, 458.

(45) Pitarke, J. M.; Silkin, V. M.; Chulkov, E. V.; Echenique, P. M. *Rep. Prog. Phys.* **2007**, *70*, 1.

(46) Johansson, P.; Monreal, R.; Apell, P. *Phys. Rev. B* **1990**, *42*, 9210.

(47) Metiu, H. *Prog. Surf. Sci.* **1984**, *17*, 153.

(48) For a structure of size a, the maximum variation of the phase of the incident field across the object is given by $\exp(ika)$. Provided $ka = 2\pi n/\lambda \ll 1$, then $\exp(ika) \simeq 1$ and $ka = \omega d/c \rightarrow 0$. Hence, transforming Maxwell's equations using $c \rightarrow \infty$ the electric field is determined by the scalar potential Φ, which satisfies the Laplace equation.[47]

(49) We assume rotational symmetry about the tip axis, thus neglecting a phase factor of the form $\cos \alpha$, with α denoting the azimuthal angle. The parameter ν is a *continuous* parameter, which requires the use of Legendre functions rather than Legendre polynomials.

(50) Using $M = \text{ArcCosh}\{(i|x| + z)/k\}$, $\eta = \cos\{Im(M)\}$, and $\xi = \cosh\{Re(M)\}$.